



HAL
open science

3D electrical imaging of the inner structure of a complex lava dome, Puy de Dôme volcano (French Massif Central, France)

Angélie Portal, Y. Fargier, Philippe Labazuy, Jean-François Lénat, Pierre Boivin, D. Miallier

► To cite this version:

Angélie Portal, Y. Fargier, Philippe Labazuy, Jean-François Lénat, Pierre Boivin, et al.. 3D electrical imaging of the inner structure of a complex lava dome, Puy de Dôme volcano (French Massif Central, France). *Journal of Volcanology and Geothermal Research*, 2019, 373, pp. 97-107. 10.1016/j.jvolgeores.2019.01.019 . hal-02024302

HAL Id: hal-02024302

<https://uca.hal.science/hal-02024302v1>

Submitted on 26 May 2021

HAL is a multi-disciplinary open access archive for the deposit and dissemination of scientific research documents, whether they are published or not. The documents may come from teaching and research institutions in France or abroad, or from public or private research centers.

L'archive ouverte pluridisciplinaire **HAL**, est destinée au dépôt et à la diffusion de documents scientifiques de niveau recherche, publiés ou non, émanant des établissements d'enseignement et de recherche français ou étrangers, des laboratoires publics ou privés.

1 **3D electrical imaging of the inner structure of a complex**
2 **lava dome, Puy de Dôme volcano (French Massif Central,**
3 **France)**

4 **A. Portal^{1,4*}, Y. Fargier², P. Labazuy¹, J.-F. Lénat¹, P. Boivin¹, D.**
5 **Miallier³**

6
7 [1] {Université Clermont Auvergne, CNRS, IRD, OPGC, LMV, F-63000 Clermont-Ferrand,
8 France}

9 [2] {GERS, IFSTTAR, Bron, France}

10 [3] {Université Clermont Auvergne, CNRS–IN2P3, LPC, F-63000 Clermont-Ferrand, France}

11 [4] {BRGM, DRP/IGT, 3 avenue Claude Guillemin, BP 36009, 45060 Orléans, France}

12 * Corresponding author at: BRGM, 3 avenue Claude Guillemin, 45060 Orléans Cedex 2, France.
13 Tel.: +33 (0) 2 38 64 32 34
14 E-mail address: a.portal@brgm.fr

15 Key words: Lava dome; Electrical Resistivity Tomography; 3D inversion; Puy de Dôme
16 volcano

17 **Abstract**

18 Lava domes result from extrusion of massive lava, frequent explosions and
19 collapses. This contribution focuses on a complex trachytic lava dome, the Puy de
20 Dôme volcano, located in the Chaîne des Puys volcanic field (French Massif Central,
21 France). We performed Electrical Resistivity Tomography (ERT) acquisitions on the
22 entire edifice in order to investigate its overall inner structure as well as to detail its
23 summit area. The resulting large ERT dataset integrated a recently developed 3D
24 inversion code based on an unstructured discretization of the geometrical model. The
25 3D inversion models obtained refine the existing geological model of the Puy de
26 Dôme's inner structure obtained by previous geophysical studies. These results also
27 highlight the strong fracturing and fumarolic alteration that affect the summit part of
28 the volcano.

29 **1. Introduction**

30 Volcanic lava domes are complex structures built up by highly viscous magmas
31 and formed by both intrusion and extrusion processes. During their growth,
32 gravitational instabilities create talus formed by rockfalls, and large collapses may

33 trigger explosive eruptions (e.g. Mount St Helens 1980, Christiansen and Peterson,
34 1981; Soufrière Hills, Herd et al., 2005) and pyroclastic flows (e.g. Unzen volcano
35 1991, Sato et al., 1992). Because their construction is often incremental and/or
36 polyphase, lava domes are usually compound edifices. Even in the case of
37 composite lava domes whose construction has been monitored, their inner structure
38 remains difficult to establish because of the intercalation of massive lava, talus
39 breccia and pyroclastites, and also because endogenous processes, such as magma
40 intrusion or hydrothermal activity, cannot be observed at the surface. Nevertheless,
41 an understanding of volcanic dome construction and evolution is an important issue
42 for hazard assessment.

43 Here, we have used the Electrical Resistivity Tomography – ERT - method to
44 study the internal structure of a large Holocene lava dome, the Puy de Dôme, in the
45 French Massif Central. The ERT technique, initially developed for environmental
46 investigations and engineering (Chambers et al., 2006; e.g. Dahlin, 1996; Loke et al.,
47 2013 and references therein), is now widely used in volcanology (e.g. Barde-
48 Cabusson et al., 2014; Brothelande et al., 2015; Byrdina et al., 2018; Fikos et al.,
49 2012; Gresse et al., 2017; Soueid Ahmed et al., 2018). As a large range of resistivity
50 values is expected in lava domes, this imaging technique is well suited to the study of
51 their inner structure, as shown by the example of La Soufrière de Guadeloupe lava
52 dome (Brothelande et al., 2014; Lesparre et al., 2014; Nicollin et al., 2006).

53 This study presents the main results from ERT surveys performed on the Puy
54 de Dôme volcano between 2011 and 2014. Given the spatial geometry of the
55 datasets, we were able to carry out a 3D inversion approach, in order to better
56 constrain the inner structure of the volcano. For this purpose, we used a recent
57 inversion code developed by Fargier et al. (2017). Our inversion strategy was first to
58 study the whole lava dome, and then to focus on its summit area only. The geological
59 interpretation of the 3D inversion models provides new information about the dome's
60 inner structure. We propose a comparison between electrical resistivity models and
61 results obtained from gravity and magnetic measurements (Portal et al., 2016) and
62 discuss the synthetic geological model of the Puy de Dôme volcano.

63 **2. Geological and structural settings**

64 The Puy de Dôme volcano is located in the Chaîne des Puys volcanic field, the
65 most recent manifestation of the French Massif Central volcanism, composed of

66 around 80 aligned Quaternary monogenetic volcanoes (scoria cones, lava domes
67 and maars) (Boivin et al., 2017). The Puy de Dôme, an 11,000 years old trachytic
68 lava dome, is the largest edifice of the volcanic chain with an elevation of 1465 m, a
69 basal diameter between 1.5 and 2 km and an apparent height of 400 m (**Fig. 1**). The
70 dome is emplaced into a cluster of several scoria cones and their associated lava
71 flows (Boivin et al., 2017; Miallier et al., 2010; Portal et al., 2016). Geological studies,
72 based on field observations, initially propose a three-stage construction model for the
73 Puy de Dôme growth (Camus, 1975): 1) the growth of a first cumulo-dome, 2) the
74 partial destruction of its eastern part and 3) the growth of a second lava spine into the
75 resulting collapse scar. Recent works modify this model and suggest that the eastern
76 flank would result from a change in the eruptive dynamism and not from a flank
77 collapse (Boivin et al., 2017). Miallier et al. (2010) propose that the dome eruption
78 ended with a final explosive activity interpreted as a summit
79 phreatic/phreatomagmatic eruption. The rock alteration on several outcrops in the
80 summit area prove that a strong hydrothermal activity accompanied the Puy de
81 Dôme growth. Debris and/or pyroclastic flows also occurred as shown by the fans of
82 unconsolidated materials observed at the base of the volcano (Portal et al., 2016).
83 Finally, Boudon et al. (2015) suggest that the hydrothermal activity progressively led
84 to a silicified permeable lava dome through cristobalite deposition into the pores and
85 deep-seated fractures.

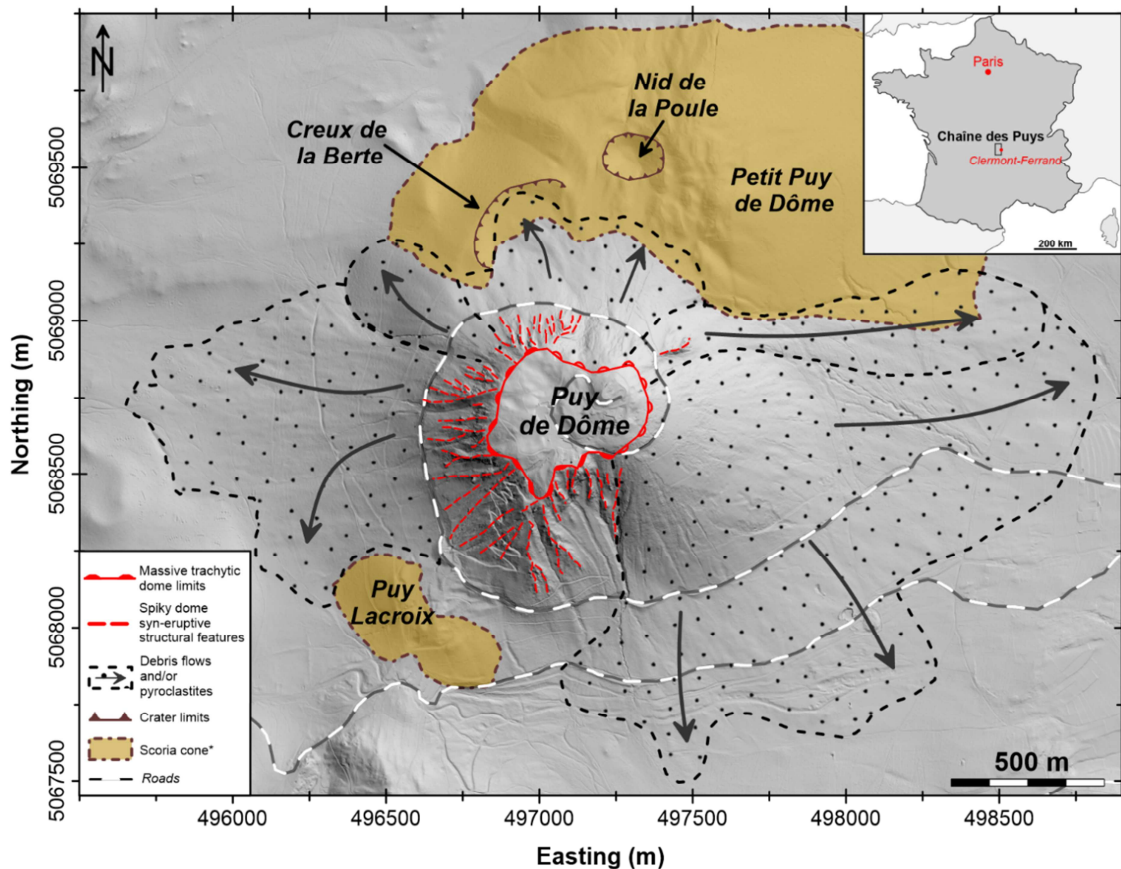


Fig. 1. Simplified map of the main morphological features observed on the Puy de Dôme volcano and its surrounding after the analysis of the high resolution DTM by Portal et al. (2016). The scoria cones limits are identified from Boivin et al. (2017). Coordinates: WGS84 – UTM31N.

86 The geological interpretation of the recent geophysical results (gravity and
 87 magnetism) obtained by Portal et al. (2016) suggests that:

- 88 1. The upper part of the lava dome could be constituted of a carapace of solid
 89 rocks, that is morphologically well-defined in the western part (**Fig. 1**);
- 90 2. The eastern flank of the volcanic dome, very regular from the top to the base
 91 could be buttressed, in its summit part, by an underlying massive carapace
 92 of rocks or welded pyroclastites;
- 93 3. The central part of the dome might be composed of successive massive
 94 intrusions and extrusions of trachyte interbedded with collapse breccia.

95 **3. ERT measurements**

96 **3.1. Data acquisition**

97 We performed twelve ERT profiles of different lengths on the Puy de Dôme

98 volcano, between 2011 and 2014 (**Table 1**). The goal was to investigate the
99 geological structures at different scales (the entire edifice on the one hand and its
100 summit area on the second hand). We defined a unique central point at the top of
101 the volcano through which we connected all the profiles crossing the area. We used
102 a multi-electrode ABEM system (Terrameter SAS 4000) associated with an
103 electrode selector (ES10-64) for data acquisitions. A standard ERT configuration
104 was composed of 64 stainless steel electrodes. To improve ground/electrode
105 contact we used clay and salty water. We applied the Wenner-alpha and Wenner-
106 Schlumberger protocols due to their good signal-to-noise ratio, their optimal depth
107 of investigation and their sensitivity to horizontal and vertical geological contrasts
108 (Dahlin et Zhou, 2004). We acquired every measurement at least three times, in
109 order to calculate a standard deviation on the data. A standard deviation value
110 greater than 5% (threshold fixed by the operator) led to additional measurements
111 (up to 4 stacks).

112 ERT lines were first deployed at the scale of whole dome (**Fig. 2a**). Two
113 perpendicular profiles allowed us to explore its inner structure (**Table 1**): an
114 approximately N-S 35 m electrode-spacing line (P1, 2.2 km-long) and a W-E line
115 (P2-1, 2.2 km-long), the latter performed in two stages. Indeed, an equipment
116 problem affected the measurements along the eastern part of the initial P2-1 profile
117 (beyond the 32th electrode). This led to data with very low signal-to-noise ratio that
118 we eliminated. To complete the truncated P2-1 dataset, we deployed a new line
119 from the summit to the volcano's eastern base (P2-2, 64 electrodes, 10 m electrode
120 spacing). We performed this 1.3 km-long line using two half-length roll-along. This
121 strategy results in a depth of investigation greater in the western part than in the
122 eastern one. Last, we performed two supplementary profiles on the southern flank
123 (P3) and at the eastern base (P4) of the volcano (**Fig. 2** and **Table 1**).

	Name	Date	Number of electrodes	Electrode spacing (m)	Coordinates (m, WGS84 - UTM31N)			
					Start electrode		End electrode	
					X	Y	X	Y
Whole dome	P1	06/2011	64	35	497466.54	5069700.19	496750.96	5067823.45
	P2-1	06/2013	32	35	496175.36	5069129.13	497075.61	5068754.54
	P2-2*	04/2014	128	10	497094.13	5068743.52	498169.52	5068440.54
	P3	04/2014	64	10	497094.77	5068739.40	497254.84	5068236.55
	P4	04/2014	64	10	497804.31	5068989.46	498043.67	5068428.31
Summit area	P5*	06/2011	128	5	497177.05	5069013.00	496953.86	5068473.31
	P6*	06/2011	128	5	496839.90	5068887.82	497380.95	5068691.14
	P7°	01/2014	51	10	496962.63	5068997.07	497183.99	5068589.63
	P8°	01/2014	64	5	497018.52	5068873.90	497173.54	5068606.14
	P9°	04/2014	64	10	496855.39	5068562.44	497325.74	5068919.28
	P10°	01/2014	64	5	496974.28	5068649.88	497214.65	5068845.12
	P11	04/2014	64	5	497054.46	5068936.99	496939.20	5068652.20

*: roll-along acquisitions ; ° and °: overlapped profiles

Table 1. Characteristics of the ERT profiles performed on the Puy de Dôme volcano, with variable electrode spacing.

124 We also carried out a detailed study of the summit area using profiles with
125 electrode spacing of 5 m (P5, P6, P8, P10 and P11) and 10 m (P7 and P9) (**Table 1**).
126 All the profiles intersecting at the same location as the long lines (**Fig. 2b**). Half-
127 length roll-along processes allowed us to extend two 5 m electrode spacing lines, P5
128 and P6. We could not expanded the P7 line beyond the 51th electrode because of the
129 presence of an access road and a railway.

130 We obtained the electrodes locations through differential GPS measurements
131 (GPS Topcon) with post-treatment of the data using the Topcon Tools software
132 (leading to centimetric precision in planimetry and altimetry). In some sectors, under
133 tree cover, we have extracted electrode elevation from the 0.5 m resolution DTM.

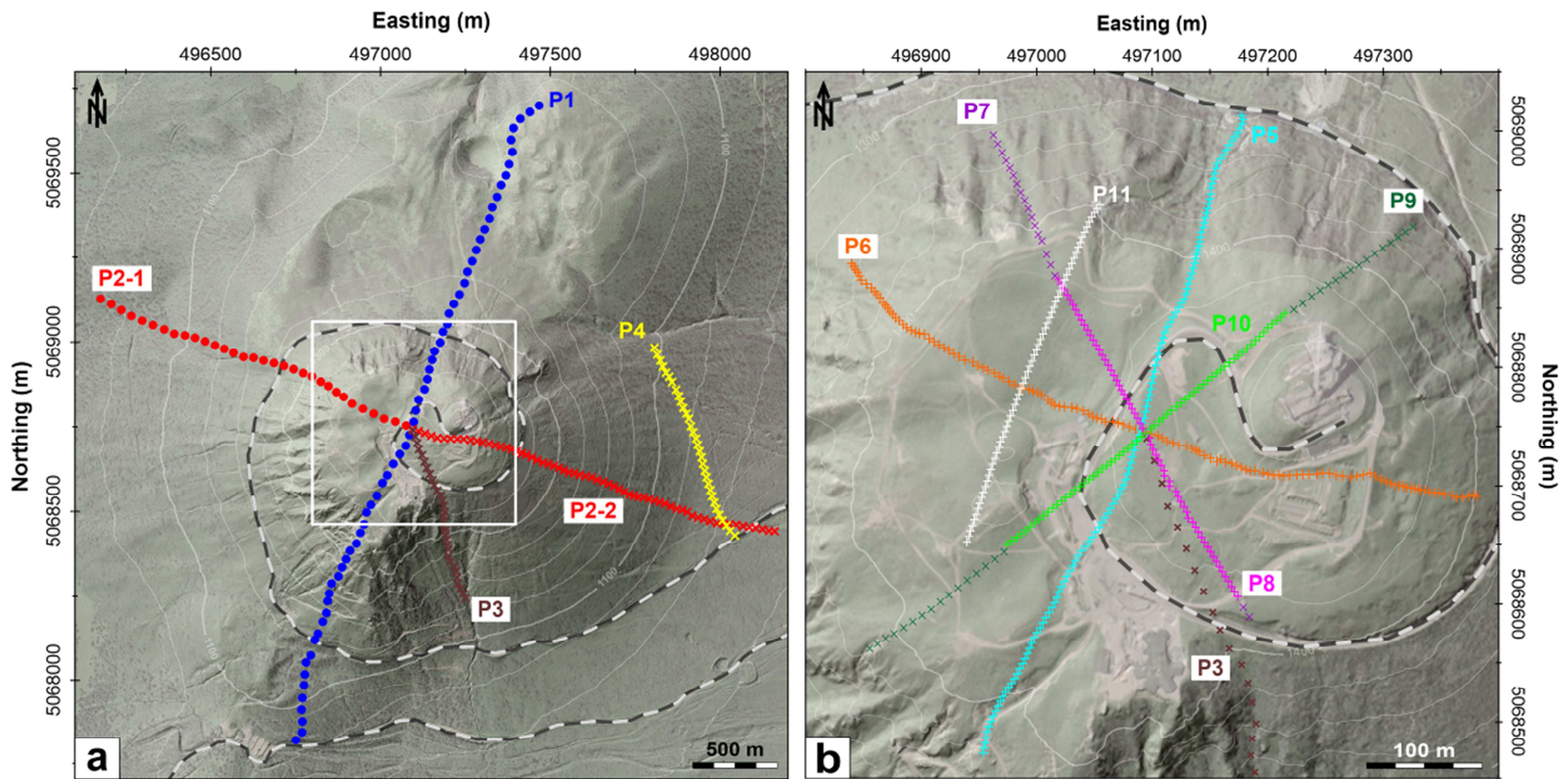


Fig. 2. (a) Location of the ERT profiles on the whole Puy de Dôme volcano. (b) Location of the ERT lines on the summit area. For P3 and P4 (a) we represent one electrode out of two. Coordinates: WGS84 – UTM31N.

3.2. Data processing and inversion

The reliability of the electrical resistivity distribution obtained from inversion models significantly depends on the data quality. Efforts were made during field measurements to lower data noise as much as possible by ensuring both good electrode/ground contacts and setting robust acquisition parameters. Several resistivity measurements were stacked and the resulting standard deviation q (also called quality factor) is less than 1% for most of the datasets. Raw resistivity data were filtered through a quality-based method (Brothelande et al., 2014), to eliminate data characterized by a low signal to noise ratio. All the measurements with an electrical potential difference of less than 1 mV and/or error higher than 5% were rejected. Before inversion, we used X2IPI software (Robain and Bobachev, 2017) to filter all datasets in order to remove artifacts due to the presence of strong heterogeneities in the shallow levels of the measurements. Finally, visualization of the data in pseudo-sections allowed us to eliminate the remaining spurious measurements.

To perform the 3D inversion of our resistivity data, we use an inversion code developed by Fargier et al. (2017). This algorithm is based on a conventional Gauss-Newton smoothness-constrained method with an Occam-type regularization (Constable et al., 1987; de Groot-Hedlin et Constable, 1990; Lines et Treitel, 1984). It also uses a non-structured discretization method (tetrahedral mesh, **Fig. 3**; Rücker et al., 2006), that is now widespread for inversion of ERT datasets, especially in volcanology (e.g. Gresse et al., 2017; Revil et al., 2010; Rosas-Carbajal et al., 2016; Soueid Ahmed et al., 2018). A complete description of this inversion code is given by Fargier et al. (2017). The RMS (Root Mean Square) error, representing the difference between the model response and the measured data, quantifies the reliability of the inversion models.

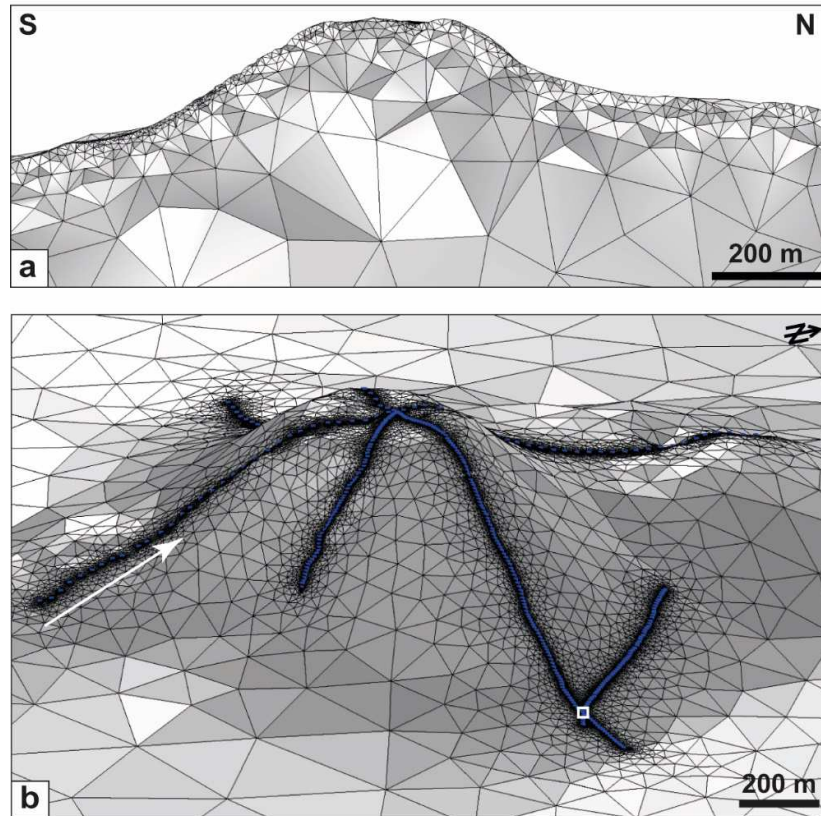


Fig. 3. (a) Vertical section in the 3D mesh along the P1, north-south oriented profile (location of this section is indicated by the white arrow on b). (b) 3D surface mesh with topography of the Puy de Dôme volcano, the blue dots represent the location of the electrodes.

161 We divide the total data set (6709 measurements) in two to perform the 3D
 162 inversion. The two derived datasets rely on the repartition and the geometry of the
 163 acquisition profiles as well as on our knowledge on the complexity of the geological
 164 structure of the dome. Thus, the first inversion named WDI (Whole Dome Inversion),
 165 integrates the ERT profiles P1 to P4 (**Table 1** and **Fig. 2a**). It aims to constrain the
 166 overall structure of the entire edifice in order to highlight the main structures inside
 167 the lava dome. The second inversion SAI (Summit Area Inversion) focuses on the
 168 summit lines P5 to P11, (**Table 1** and **Fig. 2b**) to detail the summit part of the
 169 volcano. For each inversion set, we fix a homogeneous initial model for the first
 170 iteration with a resistivity equal to the mean resistivity of the input dataset. Each
 171 following iteration uses the model of the previous one as reference. Our approach to
 172 treat the data independently (two distinct initial model) lies on the ambition to limit the
 173 propagation of error from the first model to the other.

174

175 **4. Results**

176 The inversion model of the whole Puy de Dôme (WDI) is associated to a
177 global RMS error of 7.8%. We extract horizontal sections (**Fig. 4**) and vertical ones
178 (**Fig. 7**, **Fig. 8a** and **Fig. 9a**) in the 3D model. The global RMS error of the detailed
179 3D inversion model of the summit area (SAI) is 12.7%. Horizontal (**Fig. 5**) and vertical
180 (**Fig. 6**) sections of this model have been extracted for description.

181 The presence of many man-made structures (roads, rails, paths...) affects the
182 inversion models. We identified resulting artifacts (highly conductive patches, red
183 triangles on **Fig. 6** to **Fig. 9**) that will not take part of the following
184 description/interpretation. Human activity has also strongly reworked the summit area
185 of the Puy de Dôme, as evidenced by archeological vestiges and buildings. This
186 support our choice to not describe and interpret any resistivity anomaly in the first ten
187 meters of the SAI models (**Fig. 6**). Although the inversion integrates the loss of
188 information and constraints between profiles and with depth by an increase of both
189 the tetrahedrons size (Fig. 3) and the smoothing factor, we delineate opacity masks
190 on horizontal (**Fig. 4** and **Fig. 5**) and vertical sections (**Fig. 6** and **Fig. 7**). We
191 delineate a buffer area along the profiles for the horizontal sections (the buffer
192 distance equal to twice the electrode spacing). For the vertical sections, we used the
193 data distribution with depth taking into account the topography. The objective of the
194 masks is to focus the description and interpretation of the models in the better
195 constrained areas.

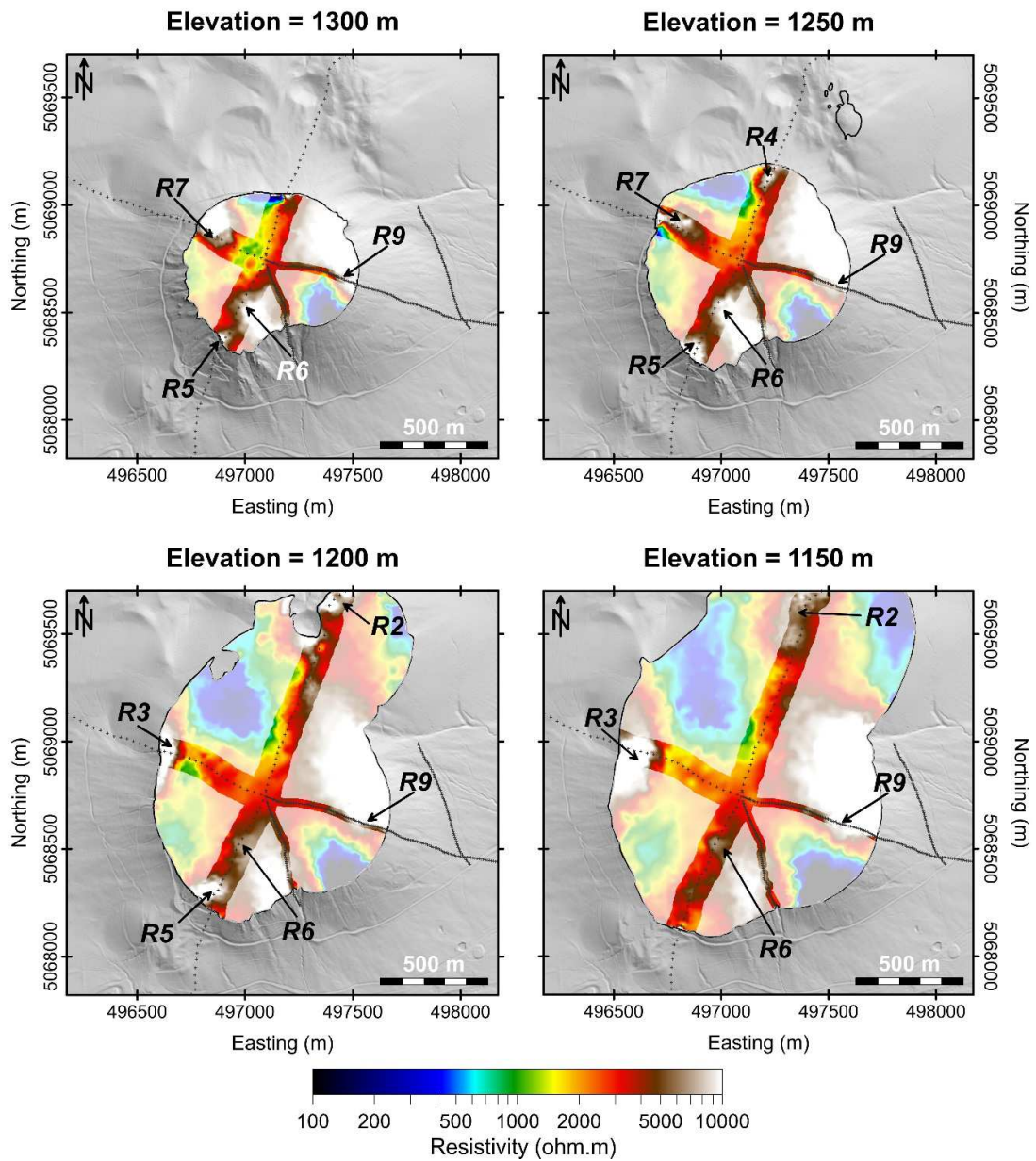


Fig. 4. Horizontal sections of the 3D inversion model of the Puy de Dôme (WDI). Sections every 50 m, starting from the elevation of 1300 m (top left) to 1150 m (bottom right). Black dots indicate the position of the electrodes. Opaque zones delineate the areas less constrained by ERT measurements. Coordinates: WGS84 – UTM31N.

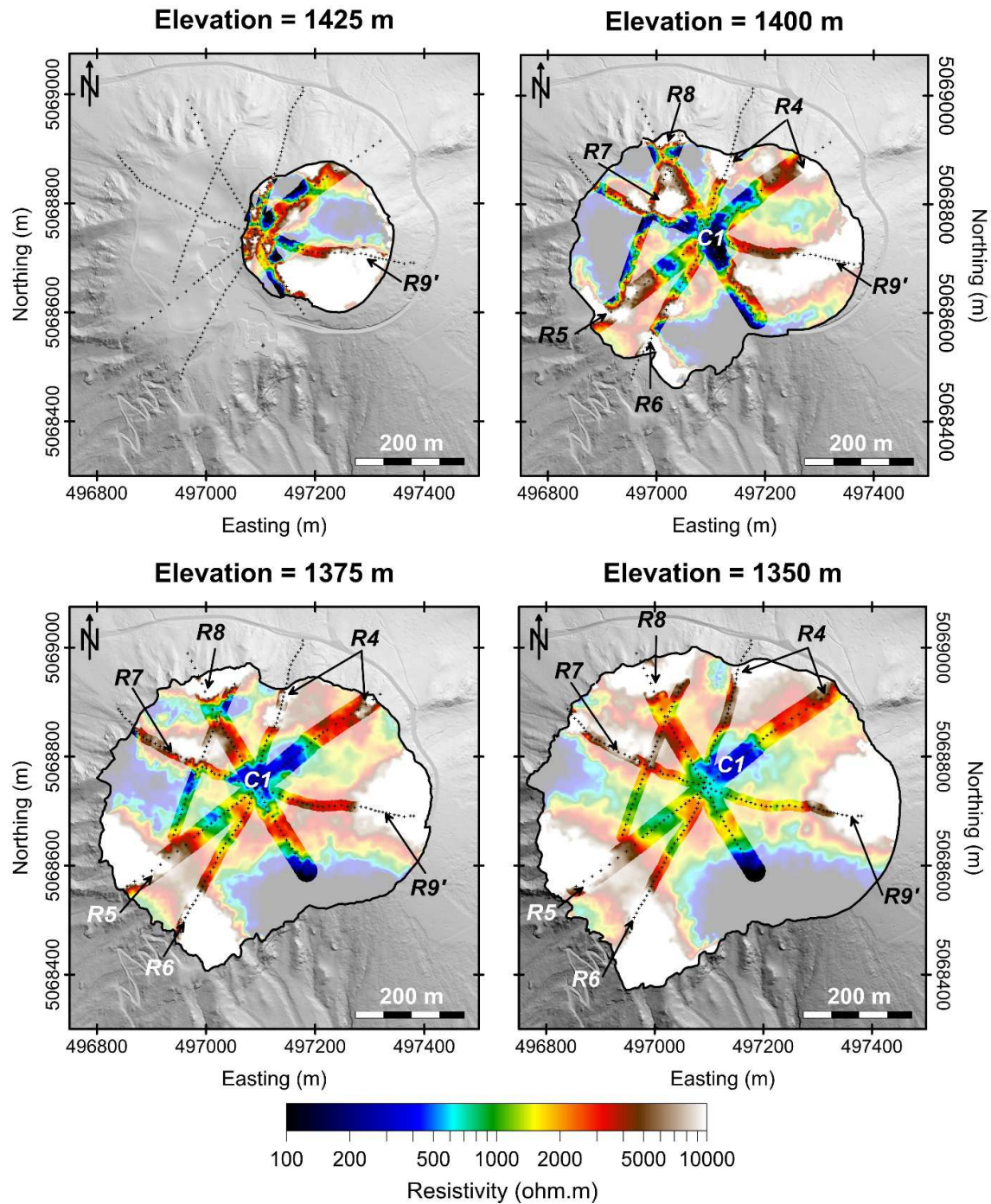


Fig. 5. Horizontal sections of the 3D inversion model of the summit area of the Puy de Dôme (SAI). Sections every 25 m, starting from the elevation of 1425 m (top left) to 1350 m (bottom right). Black dots indicate the position of the electrodes. Opaque masks delineate the areas less constrained by the ERT measurements. Coordinates: WGS84 – UTM31N.

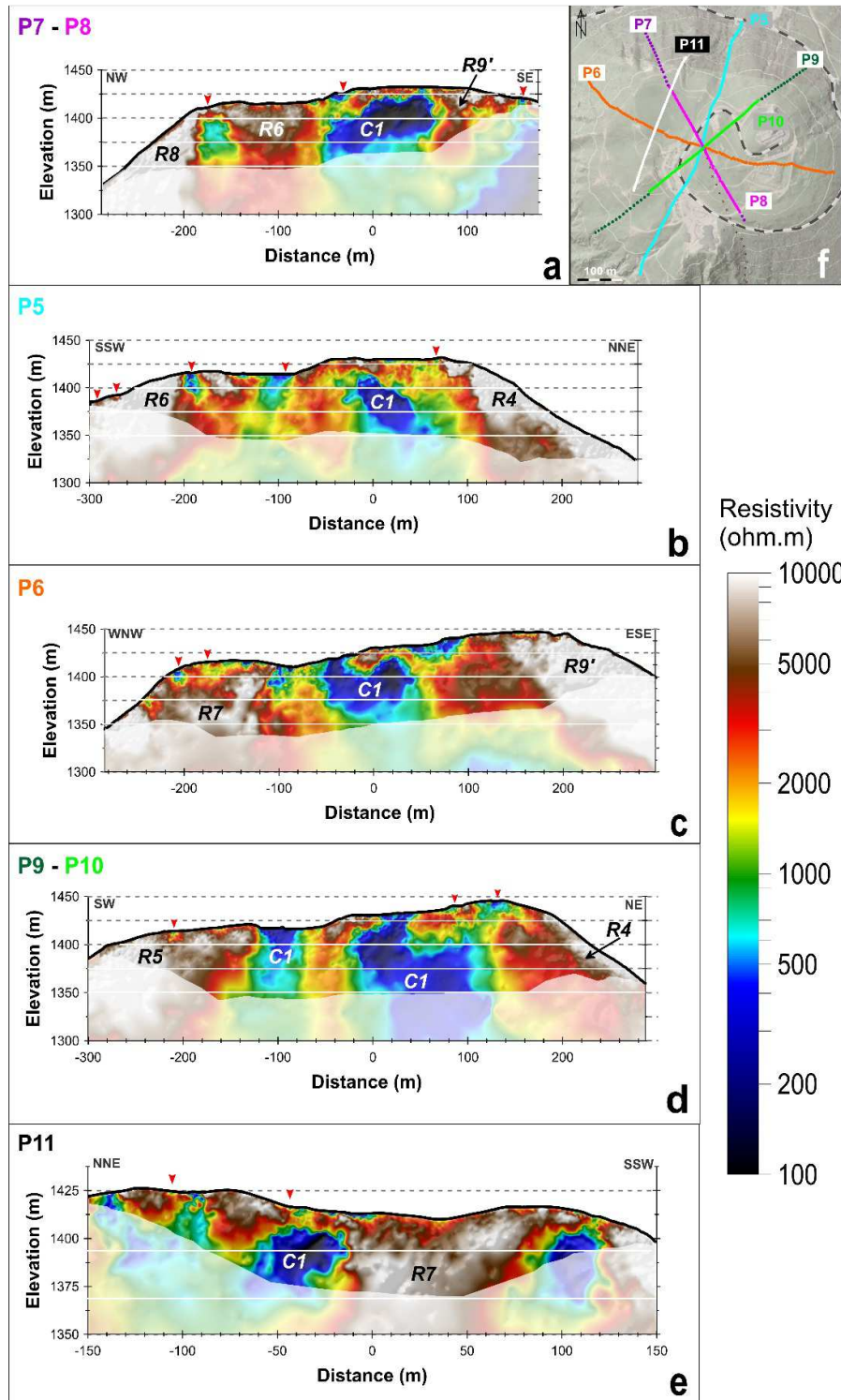


Fig. 6. Vertical sections extracted from the 3D inversion model of the summit area of the Puy de Dôme volcano (SAI): (a) P7-P8, (b) P5, (c) P6, (d) P9-P10, (e) P11. (f) Map of the location of the ERT lines. Opaque masks delineate the areas less constrained by the ERT measurements. Red triangles indicate local conductive patches associated to man-made structures (roads, paths, rail...). White lines refers to horizontal slices on **Fig. 5**. Rn and Cn represent specific features related to resistive and conductive bodies, respectively.

196 There is a wide range of resistivity variations at the scale of the Puy de Dôme,
197 from conductive values ($\rho \sim 100$ Ohm.m) to resistive ones ($\rho \sim 10$ kOhm.m). The mean
198 resistivity of the dome is about 2000-3000 Ohm.m.

199 We identify several highly resistive structures ($\rho > 5000$ Ohm.m):

- 200 - The *R1* and *R2* bodies are present near the model edges (**Fig. 4** and
201 **Fig. 8a**);
- 202 - A large highly resistive ($\rho > 9000$ Ohm.m) body, *R3*, is identified in the lower
203 part of the western flank (**Fig. 4** and **Fig. 9a**). This structure is visible around
204 an elevation of 1250 m and could extend beyond the maximum depth of
205 investigation;
- 206 - To the North, a thin and superficial (around 30 m thick, **Fig. 4** and **Fig. 8a**)
207 *R4* structure follows the slope of the volcano;
- 208 - To the South, we observe two larger highly resistive bodies. The first one,
209 *R5*, seems to be restricted to the flank (maximum thickness of 120 m). The
210 second, *R6*, reaches the surface (**Fig. 5** and **Fig. 6**) and extends inside the
211 volcano (**Fig. 7a** and **Fig. 8a**). Between an elevation 1200 m and the
212 surface, those two units progressively connect (**Fig. 4** and **Fig. 5**).
- 213 - A well-delimited resistive structure (*R7*) occupies the upper part of the
214 western flank of the lava dome (**Fig. 4**, **Fig. 5**, **Fig. 6** and **Fig. 9a**). Another
215 resistive structure body, *R8*, develops along the upper part of the NW flank
216 (**Fig. 5** and **Fig. 6**).
- 217 - Last, we highlight a very large resistive structure along and within the
218 eastern flank. We can distinguish three sub-units. The large and deep *R9*
219 (**Fig. 4** and **Fig. 8b**) structure may extends beyond the maximum depth of
220 investigation (depth > 235 m in the central part of this body). In the summit
221 area, the surface *R9'* body is around 30 m thick (**Fig. 6a**) as well as the *R9''*
222 structure at the bottom of the edifice (**Fig. 7b**).

223 A low-resistivity pattern, *C1* ($\rho < 1000$ Ohm.m), is observed in the upper part of
224 the dome, beneath the summit area (**Fig. 7a**, **Fig. 8a** and **Fig. 9a**). The horizontal
225 slices of the detailed SAI model (**Fig. 5**) show that several highly resistive bodies
226 intersect this *C1* structure.

227 The detailed summit 3D model (**Fig. 5** and **Fig. 6**) maps more accurately the
 228 main resistant structures identified on the entire dome (*R4*, *R5*, *R6*, *R7*, *R8* and *R9*).
 229 The *R7* resistive structure extends to the center part of the dome (**Fig. 6c**) and shows
 230 an elongated shape in the W-E direction (**Fig. 5**). The *R9'* unit also presents an
 231 elongated shape (at an elevation of 1400 m, **Fig. 5**) from the dome's center toward
 232 the East.

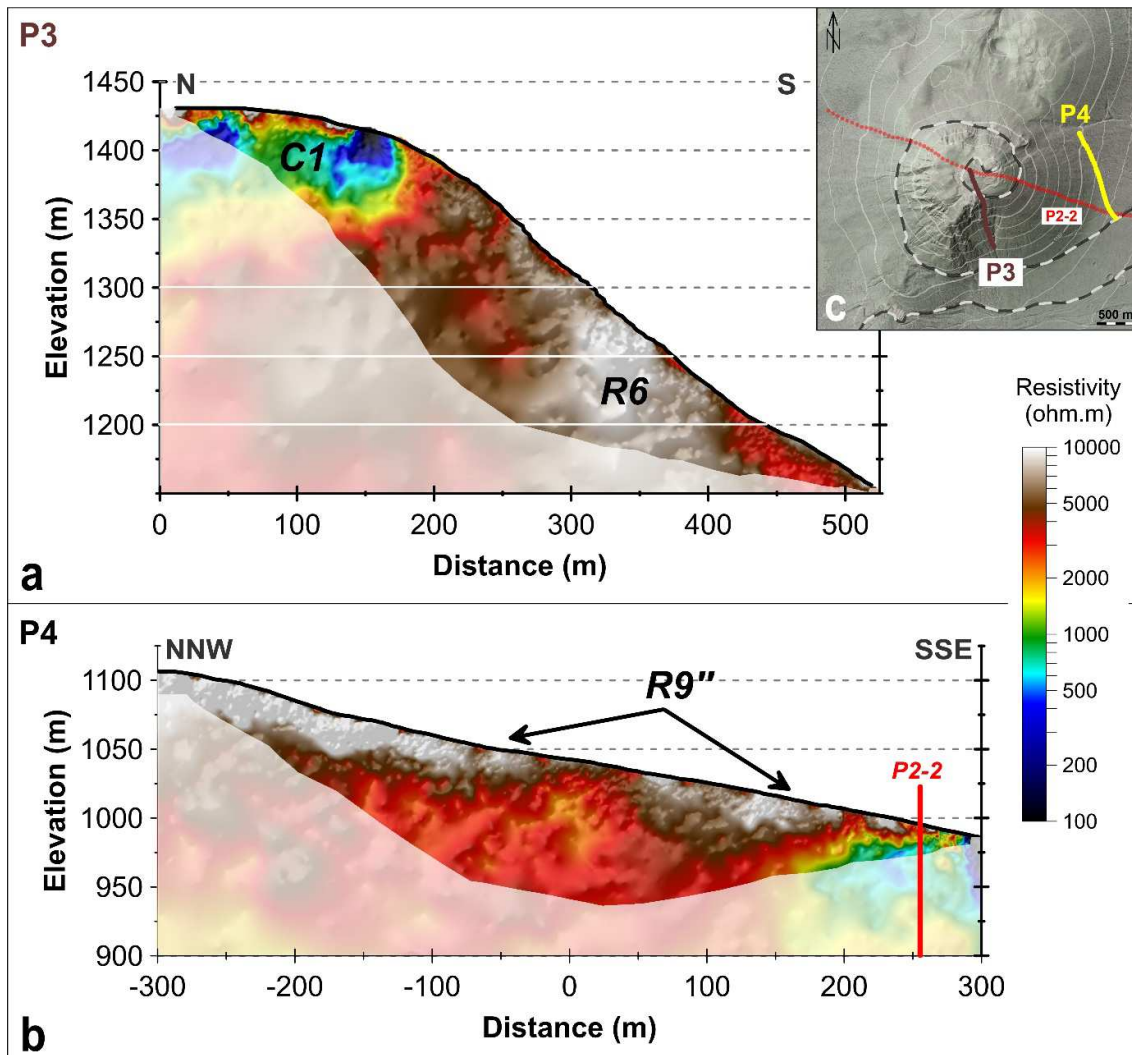


Fig. 7. Vertical sections extracted from the 3D inversion models of the entire Puy de Dôme edifice (WDI). (a) P3 profile. (b) P4 profile. (c) Map of the location of the two ERT lines. Opaque masks delineate the areas less constrained by the ERT measurements. White lines (a) refers to horizontal slices on **Fig. 4**. *R_n* and *C_n* represent specific features related to resistive and conductive bodies, respectively.

233 **5. Interpretation and discussion**

234 We base the following interpretation on the resistivity models described above,
235 while comparing them to those of the previous geophysical results (gravity and
236 magnetism, Portal et al., 2016). We first focus on the volcanic formations identified
237 below the Puy de Dôme volcano. Then, we discuss the overall structure of the lava
238 dome before concentrating on the summit part of the Puy de Dôme.

239 **5.1. The surrounding volcanic structures**

240 Within the flanks, we identify high resistivity zones ($\rho > 5000$ Ohm.m). According
241 to morphological analysis (**Fig. 1**), field observations (presence of red scoriae and
242 massive bombs) and previous geophysical results (low density body - 1.6, **Fig. 8b**
243 and **Fig. 9b**; Portal et al., 2016), we can unambiguously interpret *R1* and *R2* as
244 underlying scoria cones (the Puy Lacroix and the Petit Puy de Dôme respectively).
245 The *R3* resistive anomaly, identified on the western flank, also coincides with a low-
246 density body (1.4, Portal et al., 2016). Electric and gravity results confirm the
247 observations made by Miallier et al. (2010) who identify a buried cinder cone in this
248 area, named Cône de Cornebœufs. Our results support and confirm the theory that
249 the Puy de Dôme has grown on top of an area previously occupied by a swarm of
250 cinder cones (Boivin et al., 2017; Portal et al., 2016).

251 We observe that the dimensions of the *R1* to *R3* anomalies are more limited
252 than the dimensions of the low-density structures identified by Portal et al. (2016)
253 (**Fig. 8** and **Fig. 9**). That lets us suppose a resistivity gradient inside the low-density
254 structures, from the surface toward the lava dome's core. Considering the decrease
255 of the model resolution at depth, we can also hypothesize about a geological origin of
256 this resistivity evolution. This could correspond to an alteration of the existing scoria
257 cones by hydrothermal fluids during the lava dome's growth. Indeed, summit
258 outcrops show evidences of a former fumarolic activity (ochre alteration of the
259 trachyte). The resistivity gradient could also reflect the variation of the water content
260 in the porous scoria formations (piezometric level). However, complementary data
261 are necessary to constrain the numerical and/or the geological contribution of the
262 resistivity gradient identified in the low-density structures.

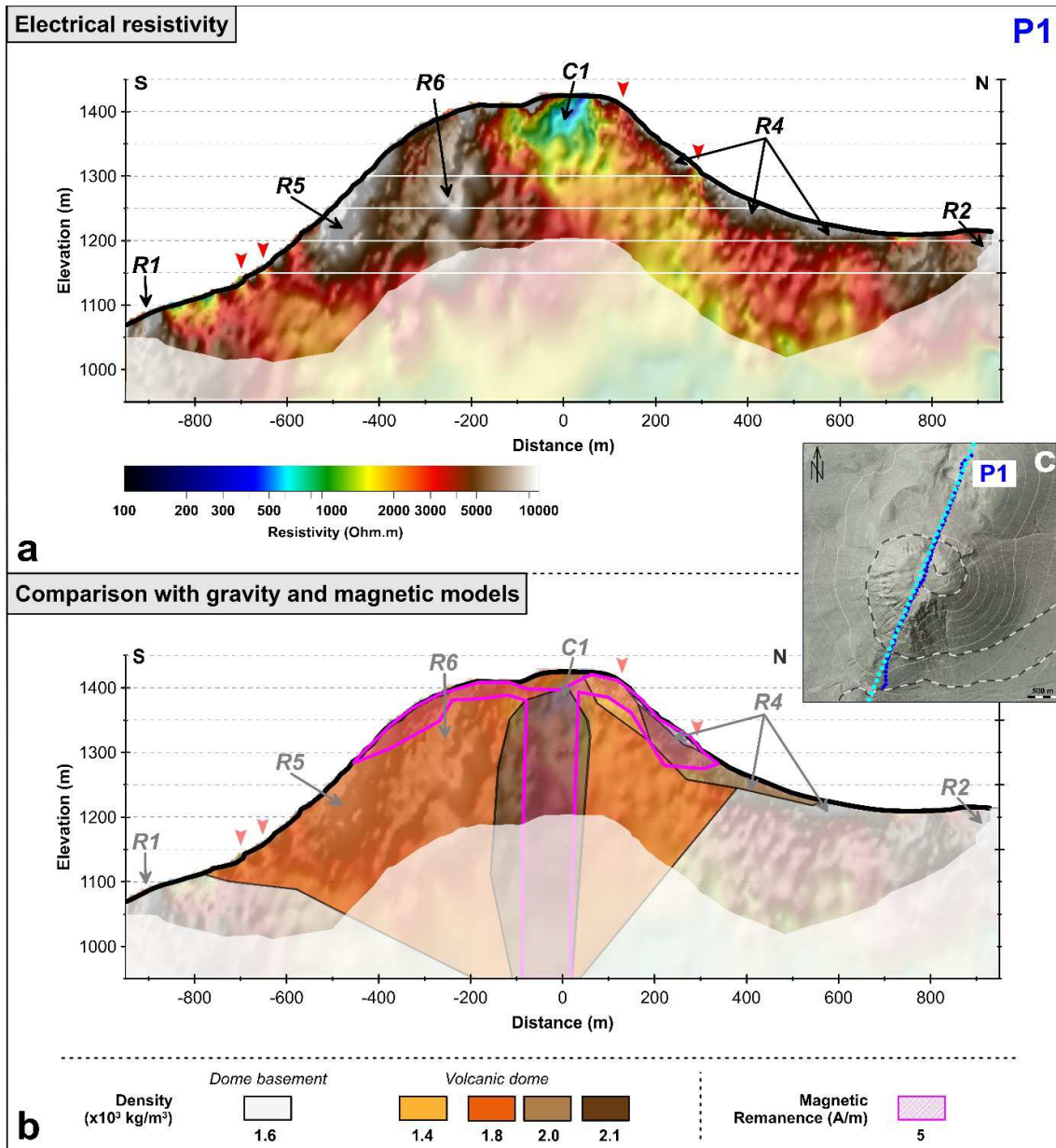


Fig. 8. (a) Vertical section extracted from the 3D inversion models of the entire Puy de Dôme edifice (Whole Dome Inversion – WDI) along the P1 ERT profile. (b) Comparison of the electrical results to the corresponding gravity and magnetic ones from (Portal et al., 2016). (c) Map of the location of the P1 line (blue) and the corresponding section extracted from gravity and magnetism results (cyan dotted line). Opaque masks delineate the areas less constrained by the ERT measurements. Red arrows indicate local conductive patches associated to man-made structures (roads, paths, rails...). White lines (a only) refer to horizontal slices on **Fig. 4**. Rn and Cn represent specific features related to resistive and conductive bodies, respectively.

263 5.2. New constrains on the overall geological structure of the lava dome

264 Overall, the resistivity structure of the Puy de Dôme itself highlights several
265 main features: (1) very high resistivity surface or shallow layers on the summit and
266 flanks, (2) an overall resistive interior and base of the edifice, and (3) a low-resistivity
267 zone in the upper part of the dome, beneath the summit area.

268 The high resistivity units *R4* (its upper part, above and elevation of 1350 m,
269 **Fig. 6b**), *R5*, *R6*, *R7*, *R8* (resistivity >5000 Ohm.m, **Fig. 4**, **Fig. 6**, **Fig. 8a** and
270 **Fig. 9a**) coincide with steeply sloping areas. Morphologically, these zones
271 correspond to surface massive trachyte ridges (**Fig. 1**), suspected to extend at
272 shallow depth. The mentioned resistive patterns correspond to low density structures
273 (1.4 to 1.6; Portal et al., 2016). The upper part of *R4* and the *R6* body also show a
274 remanent magnetization of about ~ 5 A/m (**Fig. 9b**). We suggest that these resistive
275 formations are composed of massive trachytic lava bodies. They could be former
276 lava intrusions emplaced during the construction of the spiny dome. At the scale of
277 the entire edifice, the electrical results do not highlight the presence of a massive
278 trachytic carapace as initially proposed by Portal et al. (2016).

279 The northern flank is globally less resistant (**Fig. 8a**) with no specific density or
280 magnetic signature (**Fig. 8b**). It also present a surface morphology smoother than
281 that of the southern and eastern flanks (**Fig. 1**). These observations suggest that the
282 northern flank would be composed of slightly different material probably with very few
283 or no massive lava and possibly more talus breccia. Below the elevation of 1350 m,
284 the shallow resistive pattern *R4* ($\rho > 5000$ Ohm.m) seems to be associated to an
285 intermediate density – 2.0 - structure and partially magnetized body (5 A/m, **Fig. 8b**,
286 Portal et al., 2016). This resistive formation would correspond to recent pyroclastic
287 density current deposit (Boivin et al., 2017; Portal et al., 2016). Boivin et al. (2017)
288 also describe the presence of tephra-fall deposits in this area, issued from the
289 Kilian's crater eruption, and that could contribute the *R4* resistive response.

290 Our results show that the eastern flank, whose morphology is singular (**Fig. 1**),
291 has a specific and complex high resistivity signature. Indeed, we identify the thick
292 layer *R9*, between 350 m and 850 m of distance along the profile (**Fig. 9a**) and the
293 thinner *R9'* (**Fig. 6c** and **Fig. 9a**) and *R9''* (**Fig. 7b**) bodies. In morphology, the
294 eastern flank looks like a nearly perfect half cone with a mean slope of about 33-35°

295 (Boivin et al., 2017; Portal et al., 2016). Such a value is too high for a repose angle of
296 loose material (for comparison, the nearby cinder cones have average slopes of less
297 than 25°). Boivin et al. (2017) propose that this eastern flank is mostly composed of
298 consolidated cinder deposits originating from a second exogenous eruptive phase of
299 the dome's construction. According to this hypothesis we suggest that the *R9'*, *R9''*
300 and the surface part of the *R9* (first 30 m) correspond to this welded cinder
301 pyroclastite deposits. Following this eruptive scheme, the high slopes of the eastern
302 flank could be due to an immediate induration process of the cinder products (the
303 mechanisms of such a phenomenon are still under investigation, Boivin et al., 2017).
304 The rest of the *R9* signature (below 30 m from the surface) could correspond to
305 unaltered breccia with massive lava intrusion contemporaneous to the cumulo-dome
306 construction. The lack of morphological evidences of spiky dome features along the
307 eastern flank could result from the pyroclastite emplacement that fill and cover the
308 trachyte ridges. Finally, deep inside the eastern flank of the dome, the density model
309 also suggests a low-density signature (**Fig. 9b**) interpreted as strombolian deposits
310 (Portal et al., 2016). The high resistivity observed in this area (lower part of *R9*,
311 **Fig. 9a**) support this interpretation without giving discriminating criterion.

312 The rest of the dome's inside has globally relatively high resistivity values (from
313 about 2000 Ohm.m up to 5 000 Ohm.m). Portal et al. (2016) show that these parts of
314 the dome have a generally low density (around 1.8, **Fig. 8b** and **Fig. 9b**) except the
315 presence of a dense (2.1) and magnetized (5 A/m) core. Although the model is less
316 constrained at depth, it seems that the high resistivity values observed inside the lava
317 dome support their interpretation: a conduit composed mainly of massive, poorly
318 fractured and/or altered rocks surrounded by a cogenetic breccia. The corresponding
319 high resistivity values identified suggests that the breccia probably contains former
320 massive intrusions. While the resistivity signature does not allow differentiating both
321 the breccia (low density) and the conduit (high density and magnetization), the latter
322 seems characterized by resistivity values globally slightly lower than the containing
323 formations. The hypothesis proposed here is that, along the conduit, the resistivity
324 signature may result from rock alteration due to fluid circulations during the dome
325 growth and evolution.

326 Finally, the central upper part area of the dome is very different from the flanks.
327 The sections in **Fig. 8a** and **Fig. 9a** clearly show that this zone is the most conductive

328 part of the edifice (*C1*, 100-1500 Ohm.m). On the long ERT profiles (*P1* and *P2*), the
 329 outlines of *C1* are well highlighted. However, it is with the detailed summit ERT
 330 profiles that the complex geometry and organization of this zone can be deciphered
 331 (**Fig. 6**).

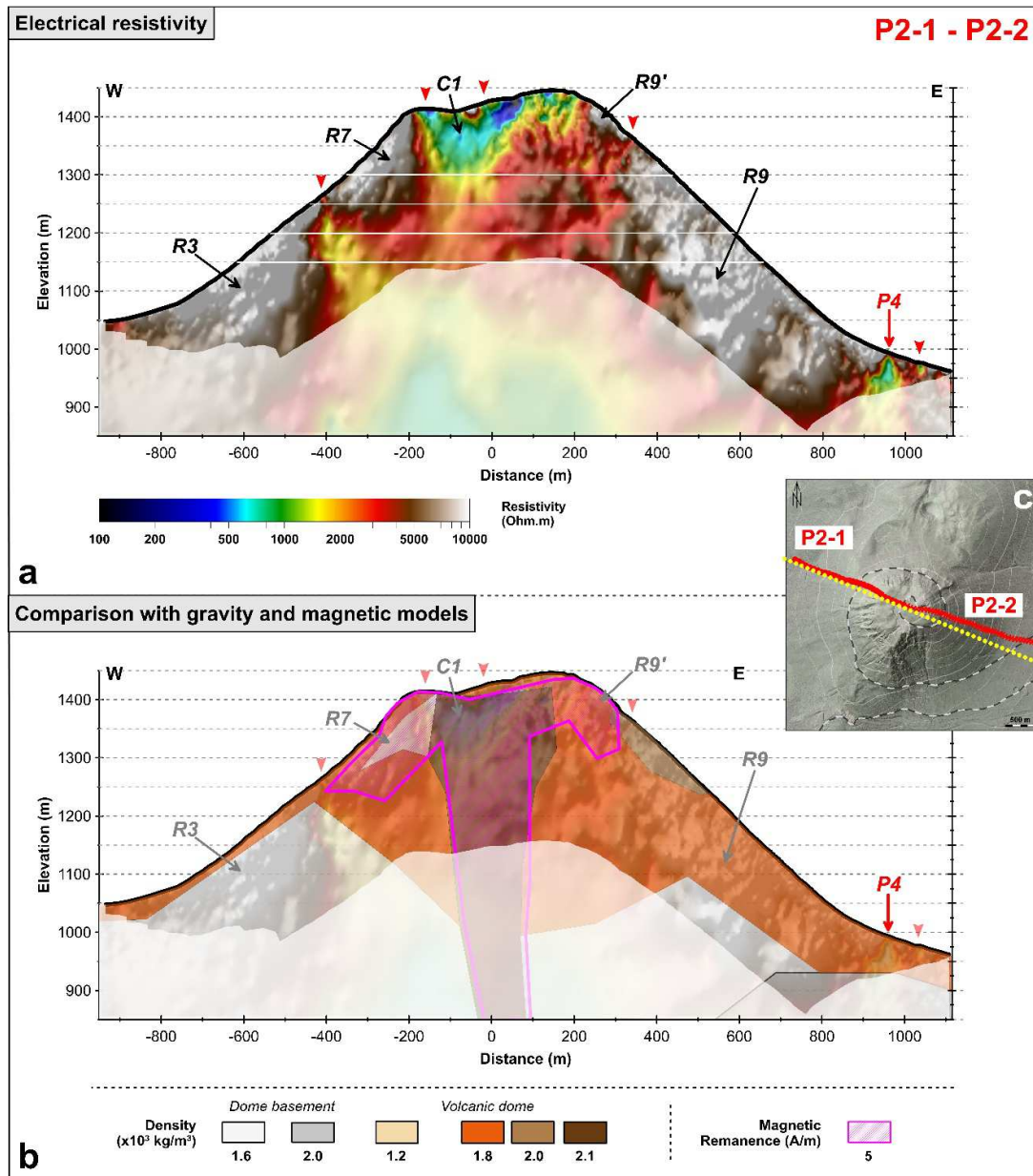


Fig. 9. (a) Vertical section extracted from the 3D inversion models of the entire Puy de Dôme edifice (Whole Dome Inversion – WDI) along the P2 ERT profile. (b) Comparison of the electrical results to the corresponding gravity and magnetic ones from (Portal et al., 2016). (c) Map of the location of the P2 line (red) and the corresponding section extracted from gravity and magnetism results (yellow dotted line). Opaque masks delineate the areas less constrained by the ERT measurements. Red arrows indicate local conductive patches associated to man-made structures (roads, paths, rails...). White lines (a only) refer to

horizontal slices on **Fig. 4**. R_n and C_n represent specific features related to resistive and conductive bodies, respectively.

332 **5.3. The complex summit area**

333 To analyze the sections in **Fig. 6**, we have to keep in mind that the thin (a few
334 meters to a few tens of meters depth), highly resistive or conductive layers in this
335 zone are strongly affected by various man-made structures and reworking.

336 The conductive zone $C1$ occupies the central part of the summit area, but its
337 shape, as well as the local variations in resistivity, are complex (**Fig. 5**). However, it
338 exhibits clear characteristics:

- 339 - Considering its dimensions and its bulk resistivity, it constitutes a major
340 structure;
- 341 - It has a maximum vertical extent of about 200 m;
- 342 - Its peripheral vertical limits are sharp;
- 343 - It may be composed of many sub-units separated by resistive structures
344 (**Fig. 5** and **Fig. 6b, c** and **d**).

345 Therefore, $C1$ could represent a single unit with resistive bodies embedded in it.
346 Field observations show evidences of small fissures and fumarolic alteration in the
347 upper part of the dome (Miallier et al., 2010; Portal et al., 2016). The hydrothermal
348 activity is commonly observed on recent or active lava domes and associated to a
349 conductive signature of the corresponding deposits (e.g. Bedrosian et al., 2007;
350 Byrdina et al., 2017; Rosas-Carbajal et al., 2016; Zlotnicki et al., 1998). We therefore
351 suggest that the $C1$ anomaly is evidence of the presence of a former hydrothermal
352 system in the upper part of the lava dome resulting into high fracturing combined to
353 an important fumarolic alteration of the rocks. Nevertheless, the comparison between
354 electrical models and results presented by Portal et al. (2016), show that this
355 conductive body $C1$ is not correlated to a specific density or magnetic pattern (**Fig. 8**
356 and **Fig. 9**). Instead, they show the presence of dense, highly magnetized rocks in
357 the central part of the dome, from the surface to possibly the base of the edifice.
358 Because the data coverage in both gravity and magnetic data is high in the summit
359 area, the shallowness of the top of the dense and magnetized bodies identified in the
360 models is reliable. Moreover, fracturing and hydrothermal fluids circulations usually
361 contribute to lower both the density and the magnetization of rocks (e.g. Bouligand et

362 al., 2014). To support resistivity, gravity and magnetic signatures, we propose the
363 following hypothesis. The fumarolic alteration is concentrated along a network of
364 small-cracks observed in the field as well as in the upper part of the deep-seated
365 fractures network identified by Boudon et al. (2015), surrounding unaltered rocks (still
366 dense and highly magnetized). In this case study, electrical results provide significant
367 arguments on the level of rock alteration in the upper part of the dome.

368 **6. Conclusion**

369 The ERT imaging of Puy de Dôme volcano aims at investigating the overall inner
370 structure of the dome as well as its summit area. The resulting datasets is large, and
371 such a density of measurement is rare regarding the study of lava domes. Here we
372 present the results of a 3D inversion of this electrical datasets as well as a
373 confrontation with complementary geophysical results from Portal et al. (2016).
374 Besides to confirm some elements of the synthetic model of the inner structure of the
375 Puy de Dôme volcano proposed by Portal et al. (2016), the geological interpretation
376 of the electrical results provide new details. The presence of massive units inside the
377 collapse breccia are evidences of former trachytic intrusions, typical of an
378 endogenous construction. Our results provide also precisions about the geometry of
379 the deposits that covered the eastern flank, which definitively excludes a major flank
380 collapse of the lava dome (Camus, 1975) and which allowed Boivin et al. (2017) to
381 propose the presence of a welded cinder deposits issued from a second exogenous
382 eruptive phase. Then, we highlight, for the first time, the boundaries of the former
383 hydrothermal system of the Puy de Dôme volcano, focused in its summit part. The
384 hydrothermal alteration also affects the feeding conduit of the lava dome, with an
385 alteration that decreases with depth.

386 More generally, this study greatly contributes to our knowledge about the
387 formation of volcanic domes although it appears difficult to draw a general model of
388 such a complex phenomenon. It seems that the magmatic feeding is concentrated
389 along an eruptive conduit. Its localization strongly depends of the volcano substratum
390 and can evolve under the pressure of the accumulated volcanic deposits. The later
391 constitute a substantial volume of the edifices as already observed during recent
392 eruptions (e.g. Soufrière Hills volcano; Wadge et al., 2009).

393 This resistivity study of a complex volcanic edifice, as well as the associated
394 gravity and magnetic study (Portal et al., 2016) are important for evaluating the
395 capacity of geophysical methods to explore the interior of a volcano, and to define
396 the best strategy to implement for that purpose. For each method, and particularly for
397 resistivity, the necessity to have good data coverage is essential to be able to derive
398 3D models and characterize structures at different scales. Even with good coverage,
399 models uncertainties can make the geological identification of structures difficult,
400 especially with increasing depth. We thus prove that collecting data, which are
401 sensitive to different physical parameters (resistivity, density and magnetization),
402 constitutes a powerful means for discriminating the geology of structures that would
403 otherwise be impossible to distinguish with one parameter (e.g. the density allows us
404 to differentiate resistive porous unsaturated rocks from scoria deposits). This case
405 study of the Puy de Dôme is therefore important at two levels: for providing
406 information about the architecture of a complex lava dome, and for guiding the
407 strategy for studying other volcanic edifices.

408 **Acknowledgements**

409 The LIDAR data used in this study derive from a collective project driven by the
410 Centre Régional Auvergnat de l'Information Géographique (CRAIG), financially
411 supported by the Conseil Départemental du Puy-de-Dôme, the European Regional
412 Development Fund and the University of Clermont-Ferrand. Datasets are available
413 on request to the authors. We thank the students and permanent staff of the
414 Laboratoire Magmas et Volcans (LMV), the TOMUVOL collaboration and the
415 Observatoire de Physique du Globe de Clermont-Ferrand (OPGC) for participation
416 and logistics during field surveys. Finally, we thank the anonymous reviewer for
417 helping comments to improve this manuscript. This research was supported by the
418 French Government Laboratory of Excellence initiative n°ANR-10-LABX-0006, the
419 Région Auvergne and the European Regional Development Fund. This is Laboratory
420 of Excellence ClerVolc contribution number 308.

421

References

- 422 Barde-Cabusson, S., Gottsmann, J., Martí, J., Bolós, X., Camacho, A.G., Geyer, A.,
423 Planagumà, L., Ronchin, E., Sánchez, A., 2014. Structural control of
424 monogenetic volcanism in the Garrotxa volcanic field (Northeastern Spain) from
425 gravity and self-potential measurements. *Bull. Volcanol.* 76, 1–13.
426 <https://doi.org/10.1007/s00445-013-0788-0>
- 427 Bedrosian, P.A., Unsworth, M.J., Johnston, M.J.S., 2007. Hydrothermal circulation at
428 Mount St. Helens determined by self-potential measurements. *J. Volcanol.*
429 *Geotherm. Res.* 160, 137–146. <https://doi.org/10.1016/j.jvolgeores.2006.09.003>
- 430 Boivin, P., Besson, J.-C., Briot, D., Deniel, C., Gourgaud, A., Labazuy, P., de
431 Larouzière, F.-D., Langlois, E., Livet, M., Médard, E., Merciecca, C., Mergoïl, J.,
432 Miallier, D., Morel, J.-M., Thouret, J.-C., Vernet, G., 2017. Volcanology of the
433 Chaîne des Puys. *Parc Nat. Régional la Chaîne des Puys (Ed.)*, Cart. Fasc. 6e
434 édition 200pp.
- 435 Boudon, G., Balcone-Boissard, H., Villemant, B., Morgan, D.J., 2015. What factors
436 control superficial lava dome explosivity? *Sci. Rep.* 5, 14551.
437 <https://doi.org/10.1038/srep14551>
- 438 Bouligand, C., Glen, J.M.G., Blakely, R.J., 2014. Distribution of buried hydrothermal
439 alteration deduced from high-resolution magnetic surveys in Yellowstone
440 National Park. *J. Geophys. Res. Solid Earth* 119, 2595–2630.
441 <https://doi.org/10.1002/2013JB010802>
- 442 Brothelande, E., Finizola, A., Peltier, A., Delcher, E., Komorowski, J.-C., Di Gangi, F.,
443 Borgogno, G., Passarella, M., Trovato, C., Legendre, Y., 2014. Fluid circulation
444 pattern inside La Soufrière volcano (Guadeloupe) inferred from combined
445 electrical resistivity tomography, self-potential, soil temperature and diffuse
446 degassing measurements. *J. Volcanol. Geotherm. Res.* 288, 105–122.
447 <https://doi.org/10.1016/j.jvolgeores.2014.10.007>
- 448 Brothelande, E., Lénat, J.-F., Normier, A., Bacri, C., Peltier, A., Paris, R., Kelfoun, K.,
449 Merle, O., Finizola, A., Garaebiti, E., 2015. Insights into the evolution of the
450 Yenkahe resurgent dome (Siwi caldera, Tanna Island, Vanuatu) inferred from
451 aerial high-resolution photogrammetry. *J. Volcanol. Geotherm. Res.* 299, 78.
452 <https://doi.org/10.1016/j.jvolgeores.2015.04.006>
- 453 Byrdina, S., Friedel, S., Vandemeulebrouck, J., Budi-Santoso, A., Suhari, Suryanto,
454 W., Rizal, M.H., Winata, E., Kusdaryanto, 2017. Geophysical image of the
455 hydrothermal system of Merapi volcano. *J. Volcanol. Geotherm. Res.* 329,
456 30–40. <https://doi.org/10.1016/J.JVOLGEORES.2016.11.011>
- 457 Byrdina, S., Grandis, H., Sumintadireja, P., Caudron, C., Syahbana, D.K.,
458 Naffrechoux, E., Gunawan, H., Suantika, G., Vandemeulebrouck, J., 2018.
459 Structure of the acid hydrothermal system of Papandayan volcano, Indonesia,
460 investigated by geophysical methods. *J. Volcanol. Geotherm. Res.* 358, 77–86.
461 <https://doi.org/10.1016/J.JVOLGEORES.2018.06.008>
- 462 Camus, G., 1975. *La Chaîne des Puys - Étude structurale et volcanologique.*
463 Université de Clermont.
- 464 Chambers, J.E., Kuras, O., Meldrum, P.I., Ogilvy, R.D., Hollands, J., 2006. Electrical

- 465 resistivity tomography applied to geologic, hydrogeologic, and engineering
466 investigations at a former waste-disposal site. *Geophysics* 71, B231–B239.
467 <https://doi.org/10.1190/1.2360184>
- 468 Christiansen, R.L., Peterson, D.W., 1981. Chronology of the 1980 eruptive activity.
469 *US Geol. Surv. Prof. Pap* 1250, 17–30.
- 470 Constable, S., Parker, R.L., 1987. Occam's inversion: A practical algorithm for
471 generating smooth models from electromagnetic sounding data. *Geophysics* 52,
472 289–300.
- 473 Constable, S.C., Parker, R.L., Constable, C.G., 1987. Occam's inversion: A practical
474 algorithm for generating smooth models from electromagnetic sounding data.
475 *Geophysics* 52, 289–300. <https://doi.org/10.1190/1.1442303>
- 476 Dahlin, T., 1996. 2D resistivity surveying for environmental and engineering
477 applications. *First Break*. <https://doi.org/10.3997/1365-2397.1996014>
- 478 Dahlin, T., Zhou, B., 2004. A numerical comparison of 2D resistivity imaging with 10
479 electrode arrays. *Geophys. Prospect.* 52, 379–398.
480 <https://doi.org/10.1111/j.1365-2478.2004.00423.x>
- 481 de Groot-Hedlin, C., Constable, S.C., 1990. Occam's inversion to generate smooth,
482 two-dimensional models from magnetotelluric data. *Geophysics* 55, 1613–1624.
483 <https://doi.org/10.1190/1.1442813>
- 484 Fargier, Y., Antoine, R., Dore, L., Lopes, S.P., Fauchard, C., 2017. 3D assessment of
485 an underground mine pillar by combination of photogrammetric and geoelectric
486 methods. *GEOPHYSICS* 82, E143–E153. <https://doi.org/10.1190/geo2016-0274.1>
- 488 Fikos, I., Vargemezis, G., Zlotnicki, J., Puertollano, J.R., Alanis, P.B., Pigtain, R.C.,
489 Villacorte, E.U., Malipot, G.A., Sasai, Y., 2012. Electrical resistivity tomography
490 study of Taal volcano hydrothermal system, Philippines. *Bull. Volcanol.* 74,
491 1821–1831. <https://doi.org/10.1007/s00445-012-0638-5>
- 492 Gresse, M., Vandemeulebrouck, J., Byrdina, S., Chiodini, G., Revil, A., Johnson,
493 T.C., Ricci, T., Vilardo, G., Mangiacapra, A., Lebourg, T., Grangeon, J., Bascou,
494 P., Metral, L., 2017. Three-Dimensional Electrical Resistivity Tomography of the
495 Solfatara Crater (Italy): Implication for the Multiphase Flow Structure of the
496 Shallow Hydrothermal System. *J. Geophys. Res. Solid Earth* 122, 8749–8768.
497 <https://doi.org/10.1002/2017JB014389>
- 498 Günther, T., Rücker, C., Spitzer, K., 2006. Three-dimensional modelling and
499 inversion of dc resistivity data incorporating topography - II. Inversion. *Geophys.*
500 *J. Int.* 166, 506–517. <https://doi.org/10.1111/j.1365-246X.2006.03011.x>
- 501 Herd, R.A., Edmonds, M., Bass, V.A., 2005. Catastrophic lava dome failure at
502 Soufrière Hills Volcano, Montserrat, 12–13 July 2003. *J. Volcanol. Geotherm.*
503 *Res.* 148, 234–252. <https://doi.org/10.1016/j.jvolgeores.2005.05.003>
- 504 Lesparre, N., Grychtol, B., Gibert, D., Komorowski, J.-C., Adler, A., 2014. Cross-
505 section electrical resistance tomography of La Soufrière of Guadeloupe lava
506 dome. *Geophys. J. Int.* 197, 1516–1526. <https://doi.org/10.1093/gji/ggu104>
- 507 Levenberg, K., 1944. A method for the solution of certain problems in least squares.

- 508 Q. Appl. Math. 2, 164–168.
- 509 Lines, L.R., Treitel, S., 1984. A review of least-squares inversion and its application
510 to geophysical problems. *Geophys. Prospect.* 32, 159–186.
511 <https://doi.org/10.1111/j.1365-2478.1984.tb00726.x>
- 512 Loke, M.H., 2012. Tutorial: 2-D and 3-D electrical imaging surveys. Geotomo
513 Software, Malaysia.
- 514 Loke, M.H., Chambers, J.E., Rucker, D.F., Kuras, O., Wilkinson, P.B., 2013. Recent
515 developments in the direct-current geoelectrical imaging method. *J. Appl.*
516 *Geophys.* 95, 135–156. <https://doi.org/10.1016/j.jappgeo.2013.02.017>
- 517 Marescot, L., Rigobert, S., Palma Lopes, S., Lagabrielle, R., Chapellier, D., 2006. A
518 general approach for DC apparent resistivity evaluation on arbitrarily shaped 3D
519 structures. *J. Appl. Geophys.* 60, 55–67.
520 <https://doi.org/10.1016/j.jappgeo.2005.12.003>
- 521 Marquardt, D.W., 1963. An Algorithm for Least-Squares Estimation of Nonlinear
522 Parameters. *J. Soc. Ind. Appl. Math.* 11, 431–441.
523 <https://doi.org/10.2307/2098941>
- 524 Miallier, D., Boivin, P., Deniel, C., Gourgaud, A., Lanos, P., Sforza, M., Pilleyre, T.,
525 2010. The ultimate summit eruption of Puy de Dome volcano (Chaine des Puys,
526 French Massif Central) about 10,700 years ago. *Comptes Rendus Geosci.* 342,
527 847–854. <https://doi.org/10.1016/j.crte.2010.09.004>
- 528 Nicollin, F., Gibert, D., Beauducel, F., Boudon, G., Komorowski, J.-C., 2006.
529 Electrical tomography of La Soufrière of Guadeloupe Volcano: Field
530 experiments, 1D inversion and qualitative interpretation. *Earth Planet. Sci. Lett.*
531 244, 709–724. <https://doi.org/10.1016/j.epsl.2006.02.020>
- 532 Park, S.K., Van, G.P., 1991. Inversion of pole-pole data for 3-D resistivity structure
533 beneath arrays of electrodes. *Geophysics* 56, 951–960.
534 <https://doi.org/10.1190/1.1443128>
- 535 Portal, A., Gailler, L.-S., Labazuy, P., Lénat, J.-F., 2016. Geophysical imaging of the
536 inner structure of a lava dome and its environment through gravimetry and
537 magnetism. *J. Volcanol. Geotherm. Res.* 320, 88–99.
538 <https://doi.org/10.1016/j.jvolgeores.2016.04.012>
- 539 Revil, A., Johnson, T.C., Finizola, A., 2010. Three-dimensional resistivity tomography
540 of Vulcan's forge, Vulcano Island, southern Italy. *Geophys. Res. Lett.* 37, n/a-
541 n/a. <https://doi.org/10.1029/2010GL043983>
- 542 Robain, H., Bobachev, A., 2017. X2IPI: user manual.
- 543 Rosas-Carbajal, M., Komorowski, J.-C., Nicollin, F., Gibert, D., 2016. Volcano
544 electrical tomography unveils edifice collapse hazard linked to hydrothermal
545 system structure and dynamics. *Sci. Rep.* 6, 29899.
546 <https://doi.org/10.1038/srep29899>
- 547 Rucker, C., Günther, T., Spitzer, K., 2006. Three-dimensional modelling and
548 inversion of dc resistivity data incorporating topography - I. Modelling. *Geophys.*
549 *J. Int.* 166, 495–505. <https://doi.org/10.1111/j.1365-246X.2006.03010.x>
- 550 Sato, H., Fujii, T., Nakada, S., 1992. Crumbling of dacite dome lava and generation

- 551 of pyroclastic flows at Unzen volcano. *Nature* 360, 664–666.
552 <https://doi.org/10.1038/360664a0>
- 553 Soueid Ahmed, A., Revil, A., Byrdina, S., Coperey, A., Gailler, L., Grobbe, N.,
554 Viveiros, F., Silva, C., Jougnot, D., Ghorbani, A., Hogg, C., Kiyan, D., Rath, V.,
555 Heap, M.J., Grandis, H., Humaida, H., 2018. 3D electrical conductivity
556 tomography of volcanoes. *J. Volcanol. Geotherm. Res.* 356, 243–263.
557 <https://doi.org/10.1016/j.jvolgeores.2018.03.017>
- 558 Tarantola, A., 2005. *Inverse Problem Theory*, SIAM. ed.
- 559 Tikhonov, A., Arsenin, V., John, F., 1977. *Solutions of ill-posed problems*.
- 560 Wadge, G., Ryan, G.A., Calder, E.S., 2009. Clastic and core lava components of a
561 silicic lava dome. *Geology* 37, 551–554. <https://doi.org/10.1130/G25747A.1>
- 562 Zlotnicki, J., Boudon, G., Viodé, J.P., Delarue, J.F., Mille, A., Bruère, F., 1998.
563 Hydrothermal circulation beneath Mount Pelee inferred by self potential
564 surveying. Structural and tectonic implications. *J. Volcanol. Geotherm. Res.* 84,
565 73–91. [https://doi.org/10.1016/S0377-0273\(98\)00030-4](https://doi.org/10.1016/S0377-0273(98)00030-4)